Editors' Suggestion

# Quantum Optics Measurement Scheme for Quantum Geometry and Topological Invariants

Markus Lysne,[1] Michael Schüler,[1,2] and Philipp Werner[1]
[1]Department of Physics, University of Fribourg, CH-1700 Fribourg, Switzerland
[2]Laboratory for Materials Simulations, Paul Scherrer Institute, CH-5232 Villigen PSI, Switzerland

(Received 25 January 2023; accepted 7 September 2023; published 11 October 2023)

We show how a quantum optical measurement scheme based on heterodyne detection can be used to explore geometrical and topological properties of condensed matter systems. Considering a 2D material placed in a cavity with a coupling to the environment, we compute correlation functions of the photons exiting the cavity and relate them to the hybrid light-matter state within the cavity. Different polarizations of the intracavity field give access to all components of the quantum geometric tensor on contours in the Brillouin zone defined by the transition energy. Combining recent results based on the metric-curvature correspondence with the measured quantum metric allows us to characterize the topological phase of the material. Moreover, in systems where $S_z$ is a good quantum number, the procedure also allows us to extract the spin Chern number. As an interesting application, we consider a minimal model for twisted bilayer graphene at the magic angle, and discuss the feasibility of extracting the Euler number.

DOI: 10.1103/PhysRevLett.131.156901

*Introduction.*—Geometrical and topological properties of Bloch states play an important role in modern condensed matter physics [1,2]. A prominent manifestation of a global topological property is the quantized value of the Hall conductivity, as obtained by linear response calculations [3,4]. Quantum geometry, on the other hand, refers to quantities that are local in momentum space, such as the Berry curvature and quantum metric [5]. They are related to topology, but also influence the motion of electrons in the Brillouin zone (BZ) [6,7], nonlinear optical responses [8–13], and flat-band superconductivity [14,15].

Since the relation between geometry, topology, and observable quantities is often not obvious, it is important to identify experimental probes which allow us to measure these quantities, or at least provide relevant bounds [16]. To this end, several schemes utilizing linear response for the measurement of quantum geometry have been proposed [16–20]. However, while the spectroscopy of topological states of matter using semiclassical descriptions has been studied extensively [19–24], the quantum optics side is less explored. In quantum optics, entanglement between light and matter can lead to novel phenomena [25–28], and it can imprint properties of the matter system into the photon field. Since current-current correlation functions are fundamentally linked to the quantum metric [29,30], this suggests that the study of photon correlation functions of a cavity system provides a potentially fruitful avenue for probing a material's geometrical and topological properties.

Here, we propose a quantum optical measurement scheme based on heterodyne detection [31,32]. The idea is to access general photon correlation functions inside a cavity, enabled by a coupling between the cavity and the environment, while a second photon field is superimposed on the field emitted from the cavity in order to slow down the time dependence of the signal. We demonstrate that such correlation functions can be directly related to the quantum geometric tensor, a quantity which encompasses both the Berry curvature and quantum metric. The latter is related to topology via the localization dichotomy [5,33,34]. Lastly, our method also provides an energy

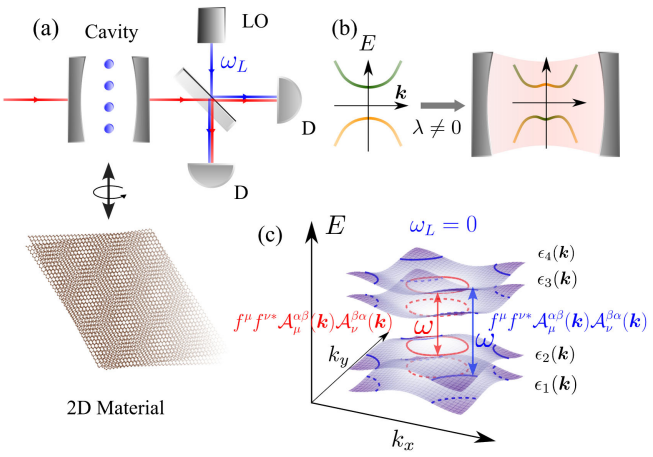


FIG. 1. (a) Proposed heterodyne detection setup with the cavity depicted on the left. The electric field exiting the cavity (red) impinges on a beam splitter along with a coherent laser source (blue) to produce a superimposed signal which is detected at two photodetectors (right and bottom right). (b) Depiction of the hybrid light-matter state arising from the cavity light-matter coupling (parameter $\lambda$). (c) $k$-space contours in a multiband model defined by a fixed excitation energy $\omega$.

 

resolution which allows us to devise useful bounds on topological invariants of 2D systems.

*Setup.*—The heterodyne detection setup is sketched in Fig. 1(a). A Fabry-Perot cavity containing a 2D material is coupled to the environment, enabling an electric field to be transmitted through it while picking up signatures of the hybrid light-matter state within the cavity [35] [Fig. 1(b)]. (To avoid complications related to edge states, we may assume that the edges of the material are outside the cavity.) By placing a 50:50 beam splitter behind the output port and superimposing a second coherent laser source—henceforth referred to as the local oscillator (LO)—it is possible to slow down the signal emitted from the cavity. This allows us to bypass limitations in the time resolution of photodetectors, which is the goal of heterodyne detection [31,32,36], and enables the measurement of various photon correlation functions in the two detectors denoted by "$D$" in Fig. 1(a) [32,36,37].

We begin by describing the intracavity Hamiltonian which can be decomposed as $\hat{H}_{\mathrm{cav}} = \hat{H}_{\mathrm{free}} + \hat{H}_I + \hat{H}_{\mathrm{mat}}$. The free cavity field is described by $\hat{H}_{\mathrm{free}} = \hbar\Omega\hat{a}^\dagger\hat{a}$, with $\hat{a}$ the photon annihilation operator and $\Omega$ the cavity frequency, while $\hat{H}_{\mathrm{mat}}$ refers to the Hamiltonian of the electron system. The light-matter coupling in the Coulomb gauge and in the single-mode approximation reads

$$\hat{H}_I = -\frac{q}{m}\hat{\boldsymbol{A}}\cdot\sum_{\boldsymbol{k},\alpha\beta}\hat{c}^\dagger_{\boldsymbol{k},\alpha}\langle\psi_{\boldsymbol{k},\alpha}|\hat{\boldsymbol{p}}|\psi_{\boldsymbol{k},\beta}\rangle\hat{c}_{\boldsymbol{k},\beta} + \frac{q^2}{2m}\hat{\boldsymbol{A}}^2\sum_{\boldsymbol{k},\alpha}\hat{c}^\dagger_{\boldsymbol{k},\alpha}\hat{c}_{\boldsymbol{k},\alpha}, \tag{1}$$

where $q$ and $m$ represent the electron's charge and mass, respectively, $\hat{\boldsymbol{A}} = \lambda[\boldsymbol{f}\hat{a} + \boldsymbol{f}^*\hat{a}^\dagger]$ the vector potential treated within the dipole approximation, $\lambda$ the light-matter coupling parameter, and $\boldsymbol{f} = (f^x, f^y)$ the mode function of the vector potential. $\hat{c}^\dagger_{\boldsymbol{k},\alpha}$ is the creation operator of an electron in the Bloch state $|\psi_{\boldsymbol{k},\alpha}\rangle$, and the material is represented in this basis by a noninteracting $N$-band model $\hat{H}_{\mathrm{mat}} = \sum_{\boldsymbol{k}}\sum_{\alpha=1}^{N}\epsilon_\alpha(\boldsymbol{k})\hat{c}^\dagger_{\boldsymbol{k},\alpha}\hat{c}_{\boldsymbol{k},\alpha}$ with $M$ occupied bands. $|u_{\boldsymbol{k},\alpha}\rangle = e^{-i\boldsymbol{k}\cdot\hat{\boldsymbol{r}}}|\psi_{\boldsymbol{k},\alpha}\rangle$ and $\epsilon_\alpha(\boldsymbol{k})$ are solutions to the eigenvalue equation $\hat{\mathcal{H}}(\boldsymbol{k})|u_{\boldsymbol{k},\alpha}\rangle = \epsilon_\alpha(\boldsymbol{k})|u_{\boldsymbol{k},\alpha}\rangle$. The light-matter coupling in the cavity gives rise to a hybrid matter-photon state, which manifests itself in the correlator of the intracavity photon mode,

$$\langle\hat{a}^\dagger(t)\hat{a}(t')\rangle - \langle\hat{a}^\dagger(t)\rangle\langle\hat{a}(t')\rangle \approx \left(\frac{q\lambda}{\hbar}\right)^2\sum_{\boldsymbol{k}}\sum_{\alpha=1}^{M}\sum_{\beta=M+1}^{N} e^{i\epsilon_{\beta\alpha}(\boldsymbol{k})t_{\mathrm{rel}}} f^\mu f^{\nu*}\mathcal{A}^{\alpha,\beta}_\mu(\boldsymbol{k})\mathcal{A}^{\beta,\alpha}_\nu(\boldsymbol{k}), \tag{2}$$

where $\langle\cdots\rangle$ is computed over the density matrix of the cavity according to the Gell-Mann low theorem [38] by adiabatically switching on $\hat{H}_I$, and $\epsilon_{\beta\alpha}(\boldsymbol{k}) \equiv (1/\hbar)[\epsilon_\beta(\boldsymbol{k}) - \epsilon_\alpha(\boldsymbol{k})]$ is the $\boldsymbol{k}$-dependent valence-conduction-band gap. $t_{\mathrm{rel}} \equiv t - t'$ and $\mathcal{A}^\mu_{\alpha\beta}(\boldsymbol{k}) = \langle u_{\boldsymbol{k},\alpha}|i\partial_\mu|u_{\boldsymbol{k},\beta}\rangle$ (with $\partial_\mu = \partial/\partial k^\mu$) the non-Abelian Berry connection. We use the Einstein summation convention for the spatial indices $\mu$, $\nu$. Equation (2) neglects a higher-order term in $\lambda$ and is valid in the regime $\Omega \ll \min_{\boldsymbol{k}\in\mathrm{BZ}}|\epsilon_{\alpha,\beta}(\boldsymbol{k})|$, i.e., away from topological transitions (see Supplemental Material [39], which includes Refs. [17,40–51], for details as well as realistic estimates of these parameters).

Our goal is to connect the intracavity correlator (2) to the detected photons in the setup of Fig. 1(a). To this end, we employ the theory of photodetection [32] and input-output theory [52], which yields

$$\frac{\overline{n(t,\Delta t)n(t',\Delta t)} - \overline{n(t,\Delta t)}\cdot\overline{n(t',\Delta t)}}{\overline{n(t,\Delta t)}} \approx \mathcal{D}\sum_{\boldsymbol{k}}\sum_{\alpha=1}^{M}\sum_{\beta=M+1}^{N}[e^{i(\epsilon_{\beta\alpha}(\boldsymbol{k})-\omega_L)t_{\mathrm{rel}}} + \mathrm{H.c.}] \times f^\mu f^{\nu*}\mathcal{A}^{\alpha,\beta}_\mu(\boldsymbol{k})\mathcal{A}^{\beta,\alpha}_\nu(\boldsymbol{k}) \tag{3}$$

for the correlations between the photon counts $n(t,\Delta t)$ at a single detector; see Supplemental Material [39]. The frequency of the local oscillator is $\omega_L$ and coefficients related to the input-output theory and beam-splitter relations are subsumed into the coefficient $\mathcal{D}$.

Equation (3) provides a direct link to the non-Abelian quantum geometric tensor (QGT),

$$\mathcal{Q}^{\alpha\beta}_{\mu\nu}(\boldsymbol{k}) = \sum_{\gamma=M+1}^{N}\mathcal{A}^{\alpha\gamma}_\mu(\boldsymbol{k})\mathcal{A}^{\gamma\beta}_\nu(\boldsymbol{k}) = g^{\alpha\beta}_{\mu\nu}(\boldsymbol{k}) - \frac{i}{2}\mathcal{F}^{\alpha\beta}_{\mu\nu}(\boldsymbol{k}), \tag{4}$$

which can be decomposed into the quantum metric $[g^{\alpha\beta}_{\mu\nu}(\boldsymbol{k})]$ and Berry curvature $[\mathcal{F}^{\alpha\beta}_{\mu\nu}(\boldsymbol{k})]$ contributions. In these expressions, $\mu,\nu = x,y$ and $\alpha,\beta\in[1,M]$. Since $f^\mu f^{\nu*}\sum_{\boldsymbol{k}}\mathrm{Tr}_b[\mathcal{Q}_{\mu\nu}(\boldsymbol{k})]$ with $\mathrm{Tr}_b[\ldots] = \sum_{\alpha=1}^{M}[\ldots]$ can be measured by Eq. (3), we gain access to (i) the Chern number if $\boldsymbol{f}_{\circlearrowright(\circlearrowleft)} = (1,\pm i)$, (ii) general diagonal components of $\mathcal{Q}$ if $\boldsymbol{f} = (1,0)$ or (0,1), and (iii) off-diagonal elements of $g$ if $\boldsymbol{f}_\pm = (1,\pm 1)$ in a way analogous to interband transitions driven by classical light [16,21,53,54].

For illustrative purposes, let us consider $\omega_L = 0$. Since $\epsilon_{\beta\alpha}(\boldsymbol{k}) > 0$, a Fourier transform of the first term on the right-hand side of Eq. (3) would select contours in the BZ with fixed energy difference $\omega$ and sum up the values of $f^\mu f^{\nu*}\mathcal{A}^{\alpha,\beta}_\mu(\boldsymbol{k})\mathcal{A}^{\beta,\alpha}_\nu(\boldsymbol{k})$ at the corresponding $\boldsymbol{k}$-points. This is shown in Fig. 1(c) for two different $\omega$'s represented by red and blue colors. The role of $\omega_L$ is to lower the frequencies at which these resonances occur, consistent with the goal of heterodyne detection [31].

*Band topology and localization dichotomy.*—The positive semidefinite nature of $\mathcal{Q}_{\mu\nu}(\boldsymbol{k})$ implies certain inequalities involving the quantum metric and topological invariants [33,55]. The inability to devise a smooth gauge

of Bloch functions in a nontrivial topological phase is an obstruction to creating maximally localized Wannier functions [56]. Since the Wannier spread is directly related to the quantum metric [34], we will utilize this localization dichotomy [57] to relate Eq. (3) to topological invariants. From now on, we will use integrals whenever discussing topological invariants, but leave the discrete sums in Eq. (2) to enable a finite system description. For Chern insulators in 2D, the localization dichotomy manifests itself in bounds for the Chern number $\mathcal{C} = (1/2\pi)\int d^2\boldsymbol{k}\mathrm{Tr}_b[\mathcal{F}_{xy}(\boldsymbol{k})]$ [33] as

$$\pi|\mathcal{C}| \leq \mathrm{vol}_g \leq \mathrm{vol}_{\tilde{g}}, \tag{5}$$

where the so-called complexity of the band $\mathrm{vol}_g = \int d^2\boldsymbol{k}\sqrt{\det\{\mathrm{Tr}_b[g(\boldsymbol{k})]\}}$ measures the BZ area with respect to the quantum metric [34] and $\mathrm{vol}_{\tilde{g}} = \sqrt{\int d^2\boldsymbol{k}\mathrm{Tr}_b[g_{xx}(\boldsymbol{k})]\int d^2\boldsymbol{k}\mathrm{Tr}_b[g_{yy}(\boldsymbol{k})] - \{\int d^2\boldsymbol{k}\mathrm{Tr}_b[g_{xy}(\boldsymbol{k})]\}^2}$. Similarly, for the most commonly studied model of twisted bilayer graphene (TBG) with two occupied bands, it has been shown [55] that

$$\frac{1}{4\pi}\int d^2\boldsymbol{k}\mathrm{Tr}_b[g_{xx}(\boldsymbol{k}) + g_{yy}(\boldsymbol{k})] \geq |e_2|, \tag{6}$$

where $e_2$ is the Euler number, a topological invariant found in models with $C_{2z}T$ symmetry [58,59]. Since $\int d^2\boldsymbol{k}\mathrm{Tr}_b[g_{\mu\nu}(\boldsymbol{k})]$ can be determined by the photon correlation measurements, Eq. (3), we can in both cases provide an upper bound to the topological invariant.

*Inequalities involving the spin Chern numbers.*—While $\mathbb{Z}_2$ insulators have zero Chern number [60,61], it is interesting to ask whether our method can provide information on the spin Chern number, which we define as $\mathcal{C}_s = \mathcal{C}_\uparrow - \mathcal{C}_\downarrow$. This is meaningful if the model Hamiltonian is of the form $\hat{\mathcal{H}}(\boldsymbol{k}) = \mathrm{diag}[h_\uparrow(\boldsymbol{k}), h_\downarrow(\boldsymbol{k})] \equiv \mathrm{diag}[h(\boldsymbol{k}), h^*(-\boldsymbol{k})]$. For such a model with time reversal symmetry (TRS) and inversion symmetry (IS), we can prove the following chain of inequalities:

$$\begin{aligned}\pi|\mathcal{C}| \leq \pi(|\mathcal{C}_\uparrow| + |\mathcal{C}_\downarrow|) = 2\pi|\mathcal{C}_\sigma| &\leq \int d^2\boldsymbol{k}\sqrt{\det\{\mathrm{Tr}_b[g(\boldsymbol{k})]\}} \\ &= 2\int d^2\boldsymbol{k}\sqrt{\det\{\mathrm{Tr}_\alpha[g^{(\alpha\sigma),(\alpha\sigma)}(\boldsymbol{k})]\}}.\end{aligned} \tag{7}$$

TRS and IS imply $g^{(\alpha\uparrow),(\alpha\uparrow)}(\boldsymbol{k}) = g^{(\alpha\downarrow),(\alpha\downarrow)}(-\boldsymbol{k})$ and $g^{(\alpha\sigma),(\alpha\sigma)}(-\boldsymbol{k}) = g^{(\alpha\sigma),(\alpha\sigma)}(\boldsymbol{k})$, which gives $g^{(\alpha\uparrow),(\alpha\uparrow)}(\boldsymbol{k}) = g^{(\alpha\downarrow),(\alpha\downarrow)}(\boldsymbol{k})$. Together with Eq. (5), this establishes that $\pi|\mathcal{C}_\sigma| \leq \frac{1}{2}\mathrm{vol}_g \leq \frac{1}{2}\mathrm{vol}_{\tilde{g}}$ (see Supplemental Material [39]).

*Improved bounds from energy resolution.*—We now explore the potential of energy-resolved measurements, as sketched in Fig. 1(c), for the extraction of the quantum geometry. The energy resolution allows us to insert additional inequalities into Eqs. (5) and (6), which enables a more complete characterization of the topology of the system. From Eq. (3) we can extract the QGT at isoenergy surfaces $\{\boldsymbol{k}\in\mathrm{BZ}, \epsilon_{\beta\alpha}(\boldsymbol{k}) - \omega_L = \omega, \alpha\in[1,M]$ and $\beta\in[M+1,N]\}$ corresponding to the contribution $\int d^2\boldsymbol{k}\sum_{\alpha,\beta}\delta(\omega - [\epsilon_{\beta\alpha}(\boldsymbol{k}) - \omega_L])f^\mu f^{\nu*}\mathcal{A}_\mu^{\alpha\beta}(\boldsymbol{k})\mathcal{A}_\nu^{\beta\alpha}(\boldsymbol{k})$. Employing the Cauchy-Schwarz inequality, we find that

$$\int_{-\infty}^{\infty} d\omega\left[\Xi_{xx}(\omega)\Xi_{yy}(\omega) - \left(\mathrm{Re}\Xi_{xy}(\omega)\right)^2\right]^{1/2} \equiv I_{\mathrm{ub}} \leq \mathrm{vol}_{\tilde{g}}, \tag{8}$$

where $\Xi_{\mu\nu}(\omega) \equiv \sum_{\alpha=1}^{M}\sum_{\beta=M+1}^{N}\int d^2\boldsymbol{k}\delta(\omega - [\epsilon_{\beta\alpha}(\boldsymbol{k}) - \omega_L])\mathcal{A}_\mu^{\alpha\beta}(\boldsymbol{k})\mathcal{A}_\nu^{\beta\alpha}(\boldsymbol{k})$. Similarly, we can derive an upper bound to $\pi|\mathcal{C}|$,

$$\pi|\mathcal{C}| \leq \int_{-\infty}^{\infty} d\omega\left|\mathrm{Im}\Xi_{xy}(\omega)\right| \equiv I_{\mathrm{lb}}. \tag{9}$$

$I_{\mathrm{lb}}$ is a strict upper bound for $\pi|\mathcal{C}|$ if $\mathrm{Im}\Xi_{xy}(\omega)$ evaluates to a negative number on certain isoenergy surfaces. Although we have established that

$$\pi|\mathcal{C}| \leq I_{\mathrm{lb}} \quad \text{and} \quad I_{\mathrm{ub}} \leq \mathrm{vol}_{\tilde{g}}, \tag{10}$$

we are only able to prove the inequality $I_{\mathrm{lb}} \leq \mathrm{vol}_g \leq I_{\mathrm{ub}}$ in the case of a two-band system. Nevertheless, the knowledge of $I_{\mathrm{lb}}$ and $I_{\mathrm{ub}}$ enables a more precise characterization of geometrical properties.

*Additional information from quantum metric bounds.*—As a minimal model of a Chern insulator, we consider the Qi-Wu-Zhang (QWZ) model [62] which corresponds to $h(\boldsymbol{k}) = \boldsymbol{d}(\boldsymbol{k})\cdot\boldsymbol{\sigma}$ with $\boldsymbol{d}(\boldsymbol{k}) = [\sin(k_x), \sin(k_y), u + \cos(k_x) + \cos(k_y)]$ in the space of $s$ and $p$ orbitals. The model displays a nontrivial phase with $|\mathcal{C}| = 1$ if the staggered onsite potential $u\in[-2,2]$, while $\mathcal{C} = 0$ otherwise. A nonzero spin-orbit coupling (SOC) can be modeled by defining $\hat{\mathcal{H}}(\boldsymbol{k}) = \mathrm{diag}[h(\boldsymbol{k}), h^*(-\boldsymbol{k})] - \Delta s_y\sigma_y$, where $s_y$ is a Pauli matrix in spin space. We will refer to this model as the SOC model in the following.

*QWZ and SOC models.*—Figures 2(a) and 2(b) show results for the model without and with spin-orbit coupling, respectively. As is evident from Fig. 2(a), the second inequality in Eq. (10) is saturated for the QWZ model, while, on the other hand, $I_{\mathrm{lb}} = \mathrm{vol}_g$ holds at most values of $u$. This is related to the metric-curvature correspondence noted in Ref. [33], which for the case of two bands is $\sqrt{\det(g)} = |\mathcal{F}_{xy}/2|$. The fact that $I_{\mathrm{lb}} = \mathrm{vol}_g$ does not hold at all values of $u$ can be attributed to sign changes of $\mathcal{F}_{xy}$ along isoenergy surfaces (see Supplemental Material [39]).

As shown in Fig. 2(b), the introduction of a small SOC $\Delta$ leads to a more pronounced peak structure of $\mathrm{vol}_{\tilde{g}}$ near

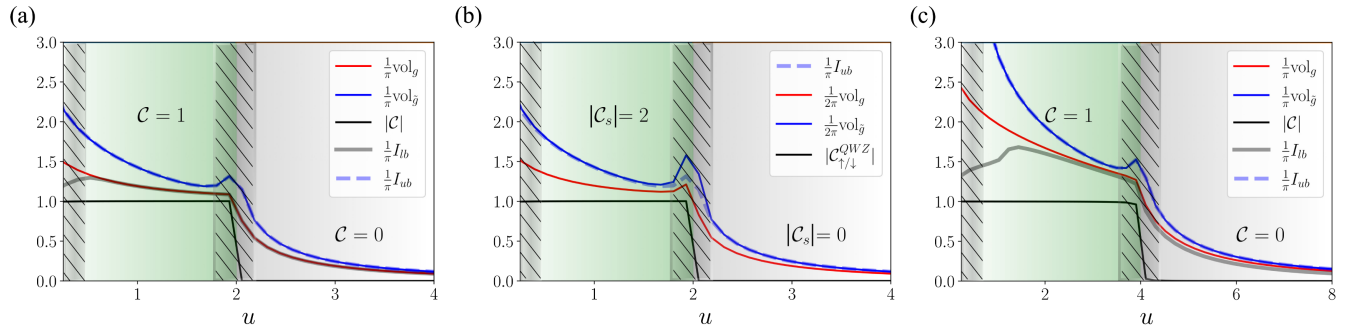


FIG. 2. Chern numbers and various bounds for (a) the QWZ model and (b) the SOC model with $\Delta = 0.1$ and (c) the result of the three-band model. All quantities of Eq. (10) are plotted as a function of the parameter $u$ which controls the topological state of the models. The hashed regions near the topological transitions roughly indicate the range of $u$ where Eq. (3) is not valid. For computing $I_{\mathrm{lb}}$ and $I_{\mathrm{ub}}$ we approximate $\delta(x)$ by $(1/\sqrt{\pi}|a|)\exp\{-(x/a)^2\}$ with $a = 0.1$.

$u = 2$. The band touching at $(\pi, \pi)$ turns into a band touching at several momentum points once the spin degeneracy of the model is lifted, which subsequently contributes to a larger QGT. Nevertheless, we still find that $(1/2\pi)\mathrm{vol}_{\tilde{g}}$ provides a useful upper bound of $\mathcal{C}_\sigma$ away from the transition.

*Three-band model.*—Next, we analyze the three-band model from Ref. [33] with $\hat{\mathcal{H}}_{11}(\boldsymbol{k}) = -2t_{dd}(\cos(k_x) + \cos(k_y)) + \delta$, $\hat{\mathcal{H}}_{12}(\boldsymbol{k}) = \hat{\mathcal{H}}_{21}(\boldsymbol{k})^* = 2it_{pd}\sin(k_x)$, $\hat{\mathcal{H}}_{13}(\boldsymbol{k}) = \hat{\mathcal{H}}_{31}(\boldsymbol{k})^* = 2it_{pd}\sin(k_y)$, $\hat{\mathcal{H}}_{22}(\boldsymbol{k}) = 2t_{pp}\cos(k_x) - 2t'_{pp}\cos(k_y)$, $\hat{\mathcal{H}}_{23}(\boldsymbol{k}) = \hat{\mathcal{H}}_{32}(\boldsymbol{k})^* = i\Delta$, $\hat{\mathcal{H}}_{33}(\boldsymbol{k}) = 2t_{pp}\cos(k_y) - 2t'_{pp}\cos(k_x)$, $t_{dd} = t_{pd} = t_{pp} = 1$, and $\delta = -4t_{dd} + 2t_{pp} + \Delta - 2t_{pp}\Delta/(4t_{pp} + \Delta)$, $t'_{pp} = t_{pp}\Delta/(4t_{pp} + \Delta)$ and compute the QGT with respect to the lowest band. Figure 2(c) shows that—similar to the QWZ model—$I_{\mathrm{lb}}$ closely follows $\mathrm{vol}_g$ over the entire trivial phase, and to some extent also in the nontrivial phase. Since $\sqrt{\det(g)}$ can differ from $|\mathcal{F}_{xy}|/2$ in models with more than two bands, $I_{\mathrm{lb}}$ is not a good estimate of $\mathrm{vol}_g$. Still, $I_{\mathrm{lb}}$ can be used to estimate the location of the topological transition with high accuracy.

*Twisted bilayer graphene.*—As a further application, we consider the four-band tight-binding model of TBG from Ref. [55],

$$\hat{\mathcal{H}}(\boldsymbol{k}) = \mu_z(\Delta\sigma_0 + \xi\sigma_z) + \mu_0\boldsymbol{\rho}(\boldsymbol{k})\cdot\boldsymbol{\sigma} - 2\lambda\mu_y\sigma_z f(\boldsymbol{k}), \quad (11)$$

where $\mu_{(0),x,y,z}$ and $\sigma_{(0),x,y,z}$ are (identity matrices) Pauli matrices acting in the space of orbital and sublattice degrees of freedom, respectively. $\rho_{1,2}(\boldsymbol{k}) = \sum_{i=1}^{3}[t\cos/\sin(\boldsymbol{\delta}_i\cdot\boldsymbol{k}) + t'\cos/\sin(-2\boldsymbol{\delta}_i\cdot\boldsymbol{k})]$, $\rho_3(\boldsymbol{k}) = 0$, and $f(\boldsymbol{k}) = \sum_{i=1}^{3}\sin(\boldsymbol{d}_i\cdot\boldsymbol{k})$. With $\boldsymbol{a}_{1,2}$ representing the real-space moiré lattice unit vectors, we have the nearest-neighbor vectors $\boldsymbol{\delta}_1 = \frac{1}{3}\boldsymbol{a}_1 + \frac{2}{3}\boldsymbol{a}_2$, $\boldsymbol{\delta}_2 = -\frac{2}{3}\boldsymbol{a}_1 - \frac{1}{3}\boldsymbol{a}_2$, $\boldsymbol{\delta}_3 = \frac{1}{3}\boldsymbol{a}_1 + \frac{2}{3}\boldsymbol{a}_2$ and the second-nearest-neighbor vectors $\boldsymbol{d}_1 = \boldsymbol{a}_1$, $\boldsymbol{d}_2 = \boldsymbol{a}_2$, $\boldsymbol{d}_3 = -\boldsymbol{a}_1 - \boldsymbol{a}_2$. In order to make the bands as flat as possible, Xie *et al.* chose $t' = -(t/3)$, $\lambda = (2/\sqrt{27})t$, and $\Delta = 0.15t$ with $t = 1$ [55]. A nonzero $\xi$ opens a gap between the otherwise degenerate occupied and unoccupied bands at $K$, rendering the topological phase trivial [see Fig. 3(a)].

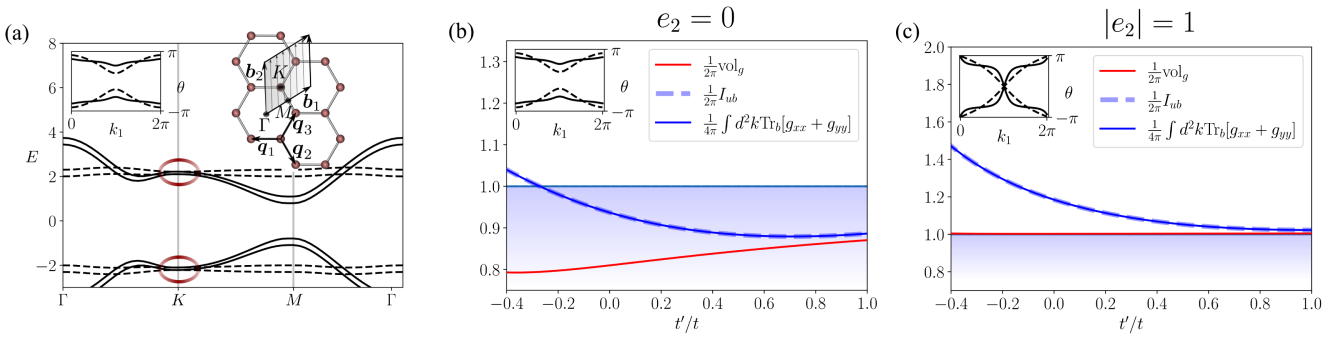


FIG. 3. Geometrical quantities for TBG plotted as a function of $t'/t$. The trivial phase is indicated with a blue shading; whenever one of the plotted quantities drops below the light-blue line, Eq. (6) implies $e_2 = 0$. (a) Band structure in the trivial phase where the nodal point at $K$ is gapped due to $\xi = 0.8$ (encircled points). (b) Trivial phase ($e_2 = 0$) with $\xi = 0.8$. The inset shows the Wilson loop in the moiré Brillouin zone for $t'/t = -0.4$ (solid) and $t'/t = 1$ (dashed) which are gapped for $\xi = 0.8$. (c) Nontrivial phase ($|e_2| = 1$) with $\xi = 0$ and unit winding of the Wilson loop for all values of $t'/t$.

The nontrivial topology in this model manifests itself in Wilson loop winding, which is seen as a crossing in the loop diagrams shown in the insets of Fig. 3 [58,63]. In the same figure, we present geometrical quantities for the two phases of the model. In view of Eq. (6), Fig. 3(b) shows that for most values of $t'/t$, we can determine whether the system is in a topologically trivial state by looking at momentum integrals over $g_{ii}$ $(i = x, y)$.

In the nontrivial case depicted in Fig. 3(c), we see the same trend of $g_{ii}$ increasing with increasing bandwidth, but notice a remarkable agreement between $(1/4\pi)\int d^2\boldsymbol{k}\mathrm{Tr}_b[g_{xx} + g_{yy}]$ and $|e_2|$ at smaller bandwidths, which is consistent with Ref. [18]. For the models considered in Ref. [33], the saturation of such inequalities was found to be related to a small bandwidth or band-gap ratio, which is consistent with the results in Fig. 3. We also observe that $(1/2\pi)\mathrm{vol}_g$ matches $|e_2|$ almost perfectly for all bandwidths in the nontrivial phase. Although the relationship between $(1/2\pi)\mathrm{vol}_g$ and $|e_2|$ is unclear, we numerically demonstrate that $(1/2\pi)\mathrm{vol}_g$ provides an upper bound to $|e_2|$ for all $t/t'$.

*Conclusions.*—We devised a way of extracting quantum geometry, and indirectly topology, by means of a cavity QED setup combined with a heterodyne detection scheme and the localization dichotomy. The power of this scheme was demonstrated with applications to paradigmatic models hosting interesting geometry and topology. Utilizing the energy resolution of the method we provided improved markers of the system's geometry. A future prospect is the application of our scheme to 3D materials (thin films) with nontrivial geometrical properties. While the Chern number is not directly determined by the Berry curvature in 3D, the delocalization of Wannier orbitals can be detected. Furthermore, in systems with Berry curvature dipoles and zero Chern number, the metric-curvature correspondence still enables a characterization of the Berry curvature dipole strength [64,65]. While the present study assumed weak light-matter coupling, strong light-matter interactions provide a pathway for engineering novel topological phases [66]. In a future project, it would thus be interesting to adapt Eq. (3) to the study of geometrical and topological properties of such hybrid light-matter states.

This work has been supported by the European Research Council through ERC Consolidator Grant No. 724103. The calculations have been performed on the Beo05 cluster at the University of Fribourg. M. S. thanks the Swiss National Science Foundation for its support with an Ambizione Grant (Project No. PZ00P2-193527).

[1] X.-L. Qi, T. L. Hughes, and S.-C. Zhang, Topological field theory of time-reversal invariant insulators, Phys. Rev. B **78**, 195424 (2008).

[2] M. Z. Hasan and C. L. Kane, Colloquium: Topological insulators, Rev. Mod. Phys. **82**, 3045 (2010).

[3] K. v. Klitzing, G. Dorda, and M. Pepper, New Method for High-Accuracy Determination of the Fine-Structure Constant Based on Quantized Hall Resistance, Phys. Rev. Lett. **45**, 494 (1980).

[4] F. D. M. Haldane, Model for a Quantum Hall Effect without Landau Levels: Condensed-Matter Realization of the "Parity Anomaly," Phys. Rev. Lett. **61**, 2015 (1988).

[5] B. Mera, A. Zhang, and N. Goldman, Relating the topology of Dirac Hamiltonians to quantum geometry: When the quantum metric dictates Chern numbers and winding numbers, SciPost Phys. **12**, 018 (2022).

[6] M. F. Lapa and T. L. Hughes, Semiclassical wave packet dynamics in nonuniform electric fields, Phys. Rev. B **99**, 121111(R) (2019).

[7] C. Leblanc, G. Malpuech, and D. D. Solnyshkov, Universal semiclassical equations based on the quantum metric for a two-band system, Phys. Rev. B **104**, 134312 (2021).

[8] Q. Ma, A. G. Grushin, and K. S. Burch, Topology and geometry under the nonlinear electromagnetic spotlight, Nat. Mater. **20**, 1601 (2021).

[9] J. Ahn, G.-Y. Guo, and N. Nagaosa, Low-Frequency Divergence and Quantum Geometry of the Bulk Photovoltaic Effect in Topological Semimetals, Phys. Rev. X **10**, 041041 (2020).

[10] J. Ahn, G.-Y. Guo, N. Nagaosa, and A. Vishwanath, Riemannian geometry of resonant optical responses, Nat. Phys. **18**, 290 (2022).

[11] J. Orenstein, J. Moore, T. Morimoto, D. Torchinsky, J. Harter, and D. Hsieh, Topology and symmetry of quantum materials via nonlinear optical responses, Annu. Rev. Condens. Matter Phys. **12**, 247 (2021).

[12] T. Morimoto and N. Nagaosa, Topological nature of nonlinear optical effects in solids, Sci. Adv. **2**, e1501524 (2016).

[13] M. Lysne and P. Werner, Nonlinear optical processes in cavity light-matter systems, Phys. Rev. B **104**, 035209 (2021).

[14] V. Peri, Z.-D. Song, B. A. Bernevig, and S. D. Huber, Fragile Topology and Flat-Band Superconductivity in the Strong-Coupling Regime, Phys. Rev. Lett. **126**, 027002 (2021).

[15] S. Peotta and P. Törmä, Superfluidity in topologically nontrivial flat bands, Nat. Commun. **6**, 8944 (2015).

[16] G. von Gersdorff and W. Chen, Measurement of topological order based on metric-curvature correspondence, Phys. Rev. B **104**, 195133 (2021).

[17] H.-T. Ding, Y.-Q. Zhu, P. He, Y.-G. Liu, J.-T. Wang, D.-W. Zhang, and S.-L. Zhu, Extracting non-Abelian quantum metric tensor and its related Chern numbers, Phys. Rev. A **105**, 012210 (2022).

[18] T. Ozawa and N. Goldman, Extracting the quantum metric tensor through periodic driving, Phys. Rev. B **97**, 201117(R) (2018).

[19] L. Asteria, D. T. Tran, T. Ozawa, M. Tarnowski, B. S. Rem, N. Fläschner, K. Sengstock, N. Goldman, and C. Weitenberg, Measuring quantized circular dichroism in ultracold topological matter, Nat. Phys. **15**, 449 (2019).

[20] D. T. Tran, A. Dauphin, A. G. Grushin, P. Zoller, and N. Goldman, Probing topology by "heating": Quantized circular dichroism in ultracold atoms, Sci. Adv. **3**, e1701207 (2017).

[21] M. Schüler and P. Werner, Tracing the nonequilibrium topological state of Chern insulators, Phys. Rev. B **96**, 155122 (2017).

[22] M. Schüler, U. De Giovannini, H. Hübener, A. Rubio, M. A. Sentef, T. P. Devereaux, and P. Werner, How Circular Dichroism in Time- and Angle-Resolved Photoemission Can Be Used to Spectroscopically Detect Transient Topological States in Graphene, Phys. Rev. X **10**, 041013 (2020).

[23] D. Baykusheva, A. Chacón, J. Lu, T. P. Bailey, J. A. Sobota, H. Soifer, P. S. Kirchmann, C. Rotundu, C. Uher, T. F. Heinz, D. A. Reis, and S. Ghimire, All-optical probe of three-dimensional topological insulators based on high-harmonic generation by circularly polarized laser fields, Nano Lett. **21**, 8970 (2021).

[24] W. Chen, Optical absorption measurement of spin Berry curvature and spin Chern marker, J. Phys. Condens. Matter **35**, 155601 (2023).

[25] M. A. Sentef, J. Li, F. Künzel, and M. Eckstein, Quantum to classical crossover of Floquet engineering in correlated quantum systems, Phys. Rev. Res. **2**, 033033 (2020).

[26] M. Ruggenthaler, N. Tancogne-Dejean, J. Flick, H. Appel, and A. Rubio, From a quantum-electrodynamical light–matter description to novel spectroscopies, Nat. Rev. Chem. **2**, 390 (2018).

[27] M. A. Sentef, M. Ruggenthaler, and A. Rubio, Cavity quantum-electrodynamical polaritonically enhanced electron-phonon coupling and its influence on superconductivity, Sci. Adv. **4**, eaau6969 (2018).

[28] F. Schlawin, D. M. Kennes, and M. A. Sentef, Cavity quantum materials, Appl. Phys. Rev. **9**, 011312 (2022).

[29] T. Neupert, C. Chamon, and C. Mudry, Measuring the quantum geometry of Bloch bands with current noise, Phys. Rev. B **87**, 245103 (2013).

[30] T. Kashihara, Y. Michishita, and R. Peters, Quantum metric on the Brillouin zone in correlated electron systems and its relation to topology for Chern insulators, Phys. Rev. B **107**, 125116 (2023).

[31] G. Grynberg, A. Aspect, and C. Fabre, *Introduction to Quantum Optics: From the Semi-Classical Approach to Quantized Light* (Cambridge University Press, Cambridge, England, 2010).

[32] W. Vogel and D.-G. Welsch, *Quantum Optics* (John Wiley & Sons, New York, 2006).

[33] T. Ozawa and B. Mera, Relations between topology and the quantum metric for Chern insulators, Phys. Rev. B **104**, 045103 (2021).

[34] N. Marzari and D. Vanderbilt, Maximally localized generalized Wannier functions for composite energy bands, Phys. Rev. B **56**, 12847 (1997).

[35] D. F. Walls and G. J. Milburn, *Quantum Optics* (Springer Science & Business Media, New York, 2007).

[36] W. Vogel, Homodyne correlation measurements with weak local oscillators, Phys. Rev. A **51**, 4160 (1995).

[37] D.-G. Welsch, W. Vogel, and T. Opatrný, II homodyne detection and quantum-state reconstruction, in *Progress in Optics* (Elsevier, New York, 1999), Vol. 39, pp. 63–211.

[38] G. Stefanucci and R. Van Leeuwen, *Nonequilibrium Many-Body Theory of Quantum Systems: A Modern Introduction* (Cambridge University Press, Cambridge, England, 2013).

[39] See Supplemental Material at http://link.aps.org/supplemental/10.1103/PhysRevLett.131.156901 for a derivation of Eq. (3) along with details related to quantum geometry and quantum optics.

[40] A. Bouhon, Q. Wu, R.-J. Slager, H. Weng, O. V. Yazyev, and T. Bzdušek, Non-Abelian reciprocal braiding of Weyl points and its manifestation in ZrTe, Nat. Phys. **16**, 1137 (2020).

[41] R. Yu, X. L. Qi, A. Bernevig, Z. Fang, and X. Dai, Equivalent expression of $F_2$ topological invariant for band insulators using the non-Abelian Berry connection, Phys. Rev. B **84**, 075119 (2011).

[42] B. A. Bernevig, Topological insulators and topological superconductors, in *Topological Insulators and Topological Superconductors* (Princeton University Press, Princeton, NJ, 2013).

[43] I. A. Sergienko and S. H. Curnoe, Order parameter in superconductors with nondegenerate bands, Phys. Rev. B **70**, 214510 (2004).

[44] R. J. Glauber, The quantum theory of optical coherence, Phys. Rev. **130**, 2529 (1963).

[45] R. Loudon, *The Quantum Theory of Light* (Oxford University Press, Oxford, 2000).

[46] N. Ismail, C. C. Kores, D. Geskus, and M. Pollnau, Fabry-Pérot resonator: Spectral line shapes, generic and related Airy distributions, linewidths, finesses, and performance at low or frequency-dependent reflectivity, Opt. Express **24**, 16366 (2016).

[47] A. Marrazzo, M. Gibertini, D. Campi, N. Mounet, and N. Marzari, Relative abundance of z 2 topological order in exfoliable two-dimensional insulators, Nano Lett. **19**, 8431 (2019).

[48] L. Talirz, S. Kumbhar, E. Passaro, A. V. Yakutovich, V. Granata, F. Gargiulo, M. Borelli, M. Uhrin, S. P. Huber, S. Zoupanos *et al.*, Materials cloud, a platform for open computational science, Sci. Data **7**, 299 (2020).

[49] K. J. Vahala, Optical microcavities, Nature (London) **424**, 839 (2003).

[50] X. Qian, J. Liu, L. Fu, and J. Li, Quantum spin Hall effect in two-dimensional transition metal dichalcogenides, Science **346**, 1344 (2014).

[51] K. Ott, S. Garcia, R. Kohlhaas, K. Schüppert, P. Rosenbusch, R. Long, and J. Reichel, Millimeter-long fiber Fabry-Perot cavities, Opt. Express **24**, 9839 (2016).

[52] C. Viviescas and G. Hackenbroich, Field quantization for open optical cavities, Phys. Rev. A **67**, 013805 (2003).

[53] D. T. Tran, A. Dauphin, A. G. Grushin, P. Zoller, and N. Goldman, Probing topology by "heating": Quantized circular dichroism in ultracold atoms, Sci. Adv. **3**, e1701207 (2017).

[54] T. Ozawa and N. Goldman, Probing localization and quantum geometry by spectroscopy, Phys. Rev. Res. **1**, 032019(R) (2019).

[55] F. Xie, Z. Song, B. Lian, and B. A. Bernevig, Topology-Bounded Superfluid Weight in Twisted Bilayer Graphene, Phys. Rev. Lett. **124**, 167002 (2020).

[56] N. Marzari, A. A. Mostofi, J. R. Yates, I. Souza, and D. Vanderbilt, Maximally localized Wannier functions: Theory and applications, Rev. Mod. Phys. **84**, 1419 (2012).

[57] D. Monaco, G. Panati, A. Pisante, and S. Teufel, Optimal decay of Wannier functions in Chern and quantum Hall insulators, Commun. Math. Phys. **359**, 61 (2018).
[58] J. Ahn, S. Park, and B.-J. Yang, Failure of Nielsen-Ninomiya Theorem and Fragile Topology in Two-Dimensional Systems with Space-Time Inversion Symmetry: Application to Twisted Bilayer Graphene at Magic Angle, Phys. Rev. X **9**, 021013 (2019).
[59] Y. Guan, A. Bouhon, and O. V. Yazyev, Landau levels of the Euler class topology, Phys. Rev. Res. **4**, 023188 (2022).
[60] C. L. Kane and E. J. Mele, $Z_2$ Topological Order and the Quantum Spin Hall Effect, Phys. Rev. Lett. **95**, 146802 (2005).
[61] B. A. Bernevig, T. L. Hughes, and S.-C. Zhang, Quantum spin Hall effect and topological phase transition in HgTe quantum wells, Science **314**, 1757 (2006).
[62] J. K. Asbóth, L. Oroszlány, and A. Pályi, A short course on topological insulators, Lect. Notes Phys. **919**, 166 (2016).
[63] Z. Song, Z. Wang, W. Shi, G. Li, C. Fang, and B. A. Bernevig, All Magic Angles in Twisted Bilayer Graphene Are Topological, Phys. Rev. Lett. **123**, 036401 (2019).
[64] S.-Y. Xu, Q. Ma, H. Shen, V. Fatemi, S. Wu, T.-R. Chang, G. Chang, A. M. M. Valdivia, C.-K. Chan, Q. D. Gibson *et al.*, Electrically switchable Berry curvature dipole in the monolayer topological insulator $WTe_2$, Nat. Phys. **14**, 900 (2018).
[65] X.-G. Ye, H. Liu, P.-F. Zhu, W.-Z. Xu, S. A. Yang, N. Shang, K. Liu, and Z.-M. Liao, Control over Berry Curvature Dipole with Electric Field in $WTe_2$, Phys. Rev. Lett. **130**, 016301 (2023).
[66] K. Masuki and Y. Ashida, Berry phase and topology in ultrastrongly coupled quantum light-matter systems, Phys. Rev. B **107**, 195104 (2023).